Nano Research Energy

ISSN 2791-0091 (print); 2790-8119 (online)
https://doi.org/10.26599/NRE.2025.9120158

Research Article

Catalytic reduction of N_2O by CO molecules using transition metal-phosphomolybdic acid (TM_1/PMA) single-atom catalysts: A theoretical perspective

Shamraiz Hussain Talib[1,2], Babar Ali[3], Arif Hassan Dar[2], Ahsanulhaq Qurashi[1,2], Jun Li[4,5] (✉), and Sharmarke Mohamed[1,2] (✉)

[1] *Center for Catalysis and Separations, Khalifa University of Science and Technology, Abu Dhabi, P.O. Box 127788, United Arab Emirates*
[2] *Department of Chemistry, Khalifa University of Science and Technology, Abu Dhabi 127788, United Arab Emirates*
[3] *Interdisciplinary Research Center for Refining and Advanced Chemicals, King Fahd University of Petroleum & Minerals, Dhahran 31261, Saudi Arabia*
[4] *Department of Chemistry, Key Laboratory of Organic Optoelectronics & Molecular Engineering of Ministry of Education, Tsinghua University, Beijing 100084, China*
[5] *Department of Chemistry, Guangdong Provincial Key Laboratory of Catalysis, Southern University of Science and Technology, Shenzhen 518055, China*

Received: 13 January 2025 / **Revised:** 26 February 2025 / **Accepted:** 1 March 2025 / **Published date:** 25 March 2025

ABSTRACT

The efficient catalytic conversion of hazardous gases (e.g., N_2O and CO) into non-harmful by products is important due to the severe environmental and health burdens posed by these gases. Here, quantum chemical studies have been carried out to investigate the catalytic reduction of N_2O by CO over a phosphomolybdic acid (PMA) cluster anchored with 3d transition metal atoms under mild reaction conditions. For N_2O reduction, all 3d-TM_1 adatoms on the PMA cluster have been systematically screened as single-atom catalysts (SACs). TM_1/PMA systems possess significant adsorption energies towards N_2O and CO, and co-adsorption energies of N_2O+CO are a necessary prerequisite for the start of the catalytic cycle. The results indicate that N_2O is decomposed first on the TM_1/PMA surface, forming N_2 and O-TM_1/PMA intermediate. The Ti_1-(0.53 eV), V_1-(0.40 eV), Cr_1-(0.86 eV), and Fe_1/PMA (0.94 eV) have low activation energy barriers that are comparable to those of the other catalysts that were chosen, making them active and selective catalysts for the N_2O decomposition. However, the remaining O atom on the TM_1/PMA was an active species for the oxidation of CO molecules. The Fe_1/PMA catalyst has an activation energy barrier of 0.43 eV and is a promising catalyst for the oxidation of CO. CO occupying the TM_1 site with stronger adsorption energy than N_2O will restrict the reaction's effectiveness. A lower temperature can hinder the generation of the side products N_2 and O_2 generated due to the disproportionation of N_2O molecules. A concerted reaction mechanism can also initiate the reaction by first adhering CO molecules to the TM_1/PMA surface. The computed activation energy barriers of the rate-limiting step are (Ti_1=0.52 eV, V_1=0.76 eV, and Fe_1=0.88 eV), respectively. Thus, 3d TM_1/PMA is predicted to be an efficient catalyst for converting toxic gases N_2O and CO into non-hazardous N_2 and CO_2 under normal conditions.

KEYWORDS

N_2O reduction, first-principles, single-atom catalysts, phosphomolybdic acid, reaction mechanism, transition metals

1 Introduction

The release of harmful gases from fossil fuel combustion, industrial activities, and vehicles is recognized as a significant problem that needs to be addressed urgently [1]. Among these, nitrous oxide (N_2O) and carbon monoxide (CO) are the two most hazardous gases, mainly released by burning fossil fuels in industry and automobile engines [2]. The issue with N_2O is twofold: it plays a significant role in global warming and has a warming potential 300 times greater than CO_2 [3]. It acts as a precursor for NO production, the primary cause of ozone depletion in the stratosphere [4]. Nitrogen oxide at high concentrations irritates the nose and eyes and affects the respiratory system [5]. It combines with atmospheric water molecules responsible for acid rain, affecting vegetation, soil, and buildings [6]. CO is another dangerous gas generated by the

© The Author(s) 2025. Published by Tsinghua University Press. The articles published in this open access journal are distributed under the terms of the Creative Commons Attribution 4.0 International License (http://creativecommons.org/licenses/by/4.0/), which permits use, distribution and reproduction in any medium, provided the original work is properly cited.

Address correspondence to Jun Li, junli@mail.tsinghua.edu.cn; Sharmarke Mohamed, sharmarke.mohamed@ku.ac.ae

incomplete combustion of fossil fuels, as well as by vehicles and industrial activities. It binds with haemoglobin in the blood, blocking oxygen transport and leading to anoxemia [7, 8]. The non-catalytic conversion of harmful gases N_2O and CO into non-harmful gases N_2 and CO_2 are not kinetically favorable because they require high activation energy [9]. Therefore, it is crucial to develop the most promising low-cost and effective catalysts to reduce and remove N_2O and CO from the environment [10].

The catalytic reduction of N_2O by CO molecule is one of the most auspicious and effective approaches since CO is low-cost and readily available [11]. Numerous experimental and theoretical reports show transition metal ions can catalyze the reduction of N_2O in the gas phase by transferring oxygen to the CO molecule [12–18]. Due to the low N_2O attraction of 40 kcal/mol, N_2O is considered an oxygen-donor molecule [19]. The substrate supported with noble metal catalysts like Pd [20], Pt [19], Ag [21], and Au [22] have been studied in detail for the reduction of N_2O. Noble metal catalysts are costly, rare, and require extremely high temperatures to facilitate reactions [23]. As a result, significant efforts have been directed toward developing non-noble metal catalysts that offer improved catalytic activity and better selectivity and operate at lower reaction temperatures for N_2O reduction [24, 25].

The reaction of oxygen transfer can be divided into two steps:

(i) The decomposition of N_2O:

$$N_2O + M^+ \rightarrow MO^+ + N_2 \quad (1)$$

(ii) The oxidation of CO:

$$MO^+ + CO \rightarrow M^+ + CO_2 \quad (2)$$

In the 1st step, the catalytic process starts with the decomposition of N_2O into N_2 and MO^+ (Eq. (1)). This is followed by a 2nd step, in which CO is oxidized to CO_2 (Eq. (2)) and the metal cation M^+ is recovered. Among the metal cations, Fe^+ has shown good catalytic activity for the N_2O reduction reaction in the gas phase. Staley and Kappes predicted that only Fe^+ can oxidize the CO molecules, while all other metal cations, such as Ti^+, V^+, Cr^+, Zr^+, and Nb^+, have not shown such activity [26, 27].

As a new branch of heterogeneous catalysis, single-atom catalysis (SACs) uses transition metal active centre's attached to metal oxide or conducting surfaces to maximize reaction selectivity and kinetics [28, 29]. Despite the dispersion on an atomic scale, industrial chemical reactions do not require the separation of catalysts after use. The SACs significantly improve catalytic efficiency and selectivity because single-atom catalysts require significantly less metal loading [29]. Reducing nanoparticle catalysts, nanoclusters, and dots to SACs significantly alters their electronic structures, bonding and coordination environments. This transformation leads to improved catalytic performance, driven solely by changes in the underlying chemical properties. In contrast, temperature and pressure strongly influence the SACs structure, whereas the catalytic activity is quenched using nanoparticle support. Metal oxide clusters are formed when metal atoms accumulate on their surfaces due to their high surface energy [30]. It is crucial to develop a microscopically smooth, highly active support surface to understand the precise nature of SACs, exclusively when working under ambient environments [31]. Numerous computational and experimental studies have found metal oxide supports are stable and effective at exercising SACs [32, 33]. The SACs show great potential in various catalytic reactions, including CO oxidation, oxygen evolution and reduction (OER/ORR), CO_2 reduction (CO_2RR), NO oxidation, and nitrogen reduction (NRR). SACs have remarkable catalytic performance, and scientists may be able to resolve scientific bottlenecks in heterogeneous catalyst-based chemical reactions by minimizing the size of the metal component until atomic dispersion is achieved.

Polyoxometalates (POMs) with kegging-like structures have been highly regarded as excellent SACs supports, primarily because of their "small island effect," which inhibits diffusion while enhancing electronic properties [34]. Phosphomolybdic acid ($H_3PMo_{12}O_{40}$, PMA) has a Keggin-type structure consisting of molybdenum and O atoms with a phosphorous atom positioned at the center of Keggin [35–39]. PMA has arisen as a superior support for single atoms to be stably embedded because of their precise structure, which has a variety of coordination sites consisting of bare O atoms [40–42]. Using a Keggin-type POMs surface with a high Pt single atom loading (around 1%), Yan's group reported the first POM-supported SACs that could catalyze the hydrogenation of cyclohexanone and nitrobenzene. According to their findings, the Pt atom stabilized by four surface oxygen atoms in the Keggin-type POMs support might be a decisive factor for high activity [43]. As a result, POMs are perfect supporting materials for SACs, providing enhanced sintering resistance and increased metal loading [44, 45]. Wang et al. calculation shows that different TM atoms embedded over the PMA surface have very high stability and possess higher binding energy compared to other commonly used metal oxide supports, indicating that they are sufficiently stable to resist aggregation [43]. A new porous ammonia salt of phosphotungstic acid (PTA) has been reported by Yan et al. to form the neutral Rh_1/PTA SACs through a strong electrostatic interaction between $[PW_{12}O_{40}]^{3-}$ and Rh^{3+} [46]. It has been reported that Rh_1/PTA SAC is very stable and performs exceptionally well in CO oxidation. According to a mechanistic analysis, CO is oxidized when the active oxygen species on PTA's surface reacts with the CO adsorbing on the Rh_1 atom. Feng et al. investigated theoretically by focusing on the geometry and stability of different TM atoms on the PMA surface at the fourfold oxygen hollow site [47, 48]. The calculated results show that TM-PMAs are the most promising catalysts for CO oxidation with high catalytic activity and selectivity. Li et al. assessed the ethylene epoxidation (C_2H_4O) reaction catalytic activity of the phosphotungstic acid (PTA) cluster with various single-atom catalysts. They found that Fe_1/PTA single atom enhanced catalytic activity under ambient reaction environments [49]. Mo_1/PMA provided the best catalytic activity in eNRR through the enzymatic mechanism of various PMA-supported SACs that were theoretically investigated for eNRR [50]. Lu et al. investigated OER/ORR reactions using single atom catalysts supported PMA cluster and found that the Co_1-, Fe_1- and Pt_1/PMA had superior catalytic performance and selectivity for OER/ORR related with other SACs [51]. To develop new POMs-supported SACs, an in-depth understanding of the surface oxidation chemistry, particularly the interface between the single metal atom and POMs support, is critical. Accordingly, future investigations and research should be devoted to this area.

Based on the results of earlier research, we conducted quantum chemical calculations using periodic density functional theory (DFT) to investigate the reduction of N_2O by CO molecules on 3d TM_1/PMA surfaces, where TM_1 represents Zn_1, Cu_1, Ni_1, Co_1, Fe_1, Mn_1, Cr_1, V_1, Ti_1, and Sc_1. The adsorption configuration, geometries, stability, and catalytic behavior of single transition metal atoms supported on the PMA surface were investigated. We

systematically explored N_2O, CO, N_2, CO_2, and co-adsorption of N_2O+CO molecules over TM_1/PMA. We found that the Ti_1/PMA and Fe_1/PMA are the most suitable catalysts for N_2O reduction. The calculated overall energy barrier is less than 1 eV. These results indicate that Ti_1- and Fe_1/PMA can be used to reduce environmentally hazardous gases. This work will be beneficial for developing economical catalysts that efficiently convert harmful gases such as CO and N_2O into non-harmful gases such as N_2 and CO_2.

2 Theoretical methods

Geometry optimization and energy calculations were performed using spin-polarized density functional theory (DFT) with the Vienna *Ab initio* Simulation Package (VASP) [52–56]. To account for interactions between core and valence electrons, the Projector Augmented Wave (PAW) method was utilized [57–59]. The calculations employed the generalized gradient approximation (GGA) with the Perdew-Burke-Ernzerhof (PBE) exchange-correlation function [54, 55, 60, 61]. Van der Waals interactions were included using Grimme's dispersion-corrected DFT-D3 method. A plane wave energy cutoff of 400 eV was set for electronic eigenfunction expansion. The polyoxometalate (PMA) surface was modelled as a supercell containing 3×3 primitive cells, which included 12 molybdenum (Mo) atoms, 40 oxygen (O) atoms, and 1 phosphorus (P) atom. A vacuum layer of 20 Å was added to eliminate interactions between the PMA surface and its periodic images. For sampling the surface Brillouin Zone (BZ), a Monkhorst-Pack k-points grid centred at the Γ-point with dimensions of 1×1×1 was applied. Ionic positions were optimized until the maximum force acting on any ion was below 0.02 eV/Å. Atomic charges were determined using Bader's quantum theory of atoms in molecules (QTAIM) [62–64].

According to thermodynamic principles, the binding energy of TM_1 atoms on the PMA is characterized as follows:

$$E_{b[TM1]} = E_{tot[TM/PMA]} - E_{[PMA]} - E_{[TM]} \quad (3)$$

In this work, the adsorption energy (E_{ads}) of an adsorbate (X) was calculated from Eq. (4):

$$\Delta E_{ads} = E_{tot[X...TM/PMA]} - E_{[TM/PMA]} - E_{[X]} \quad (4)$$

Where, $E_{tot\ [X...TM/PMA]}$, $E_{[TM/PMA]}$, and $E_{[X]}$ represent the total energy of the X…TM_1/PMA adsorption system, and TM_1/PMA is the energy of the pure catalyst and free adsorbate, respectively.

Furthermore, the coadsorption energies of N_2O and CO were calculated from Eq. (5):

$$\Delta E_{coads} = E_{tot} - E_{[TM/PMA]} - E_{[N_2O]} - E_{[CO]} \quad (5)$$

To analyze the reaction pathway and calculate energy barriers, the climbing image nudged elastic band (CI-NEB) [65, 66] and dimer methods [67–69] were employed. These techniques determine the minimum energy path, accurately identify the reaction's transition states, and compute precise reaction energy barriers. The transition state geometries were confirmed by ensuring the presence of a single imaginary vibrational frequency. All other computational parameters were set to the program's default values. According to thermodynamic principles, positive energy values indicate endothermic reactions, while negative values correspond to exothermic reactions.

3 Results and discussion

This study utilized PMA as the substrate to immobilize the individual metal atoms. The completely optimized configuration of the PMA is illustrated in Figs. 1(a) and 1(b). Keggin-type PMA are structured with 12 MoO_6 octahedrons, which share their edges or corners with a central PO_4 tetrahedron. The PMA cluster offers various coordination sites, including two 3-fold hollow sites (3H-O_c and 3H-O_{bri}), one 4-fold hollow site (4H), and a bridge site (B-O_c-O_{bri}), all of which can serve as potential binding locations (see in Fig. S1 in the Electronic Supplementary Material (ESM)). The cubic unit cell consists of 12 molybdenum (Mo) atoms, 40 oxygen (O) atoms, and a single phosphorus (P) atom at the core. Earlier studies revealed that transition metal atoms, such as Fe, Co, Ni, Cu, Pd, Rh, Ru, Ag, Os, Ir, Pt, and Au, tend to occupy the most stable 4H site on the PMA surface, adopting a distorted square planar geometry [49–51]. The main geometric parameters are summarized in Table S1 in the ESM. The calculated bond lengths for P-O, Mo-O_c, Mo-O_{bri}, and O_{bri}-O_{bri} are 1.55, 1.70, 1.93, and 2.72 Å, respectively. These results align well with those reported in previous studies [50, 51]. The 4H site provides balanced bond lengths with adjacent oxygen atoms, suggesting its ability to stabilize intermediates in multi-step processes. This phenomenon is referred to the elongation of bond lengths, indicating that the anchoring of TM_1 atoms is favoured to provide new interfaces for catalytic processes.

In this section, we first examined the adsorption of single TM_1 atoms over the PMA surface. Then, we explained the adsorption of CO, N_2O, CO_2, N_2 molecules and co-adsorption of CO+N_2O molecules over the TM_1/PMA surface. Finally, we discussed the reaction mechanisms and the energy barriers for reducing N_2O by CO molecule.

3.1 Screening of TM_1/PMA catalysts for catalytic reduction of N_2O by CO

To identify the most effective catalytic system for reducing N_2O in the presence of CO, a series of 3d transition metals (TM_1 = Sc_1, Ti_1, V_1, Cr_1, Mn_1, Fe_1, Co_1, Ni_1, Cu_1, and Zn_1) were analyzed. It was observed that all TM_1 atoms studied preferentially anchor at the 4H site on the PMA surface (Fig. S2 in the ESM). The calculated binding energies (E_b) for the TM_1/PMA surfaces range from −5 to −16 eV (see Fig. 1(c) and Table S2 in the ESM). The binding strength of TM_1 atoms to the PMA surface follows the order: Sc_1 > Ti_1 > V_1 > Cr_1 > Mn_1 > Fe_1 > Co_1 > Ni_1 > Zn_1 > Cu_1. These findings indicate that the Sc_1 atom exhibits the strongest binding interaction with the PMA surface compared to the other transition metals. Thus, due to durable interaction, the PMA surface is an excellent support for single TM_1 atom catalysts. In the PMA structure, the fitting of larger metals and their binding strength can be affected by steric hindrance. Smaller metals can access coordination sites more readily, resulting in better interactions. Along the periodic table, clear trends in the computed E_b can also be seen in Fig. 1(c). PMA's oxygen atoms form weaker bonds with metals that have occupied more d orbitals, reducing E_b magnitude. The atomic radii of 3d atoms are lower, which results in computed average bond lengths of TM_1–O bonds being less than 1.95 Å (Fig. S2 in the ESM). Catalytic sites with high (E_b) values sustain contact with TM_1 throughout the adsorption process, but those with low (E_b) values cannot form robust bonds because of unequal coordination environments. We also compare the E_b values with experimental metal cohesive energies and see a similar tendency for embedded metal atoms to

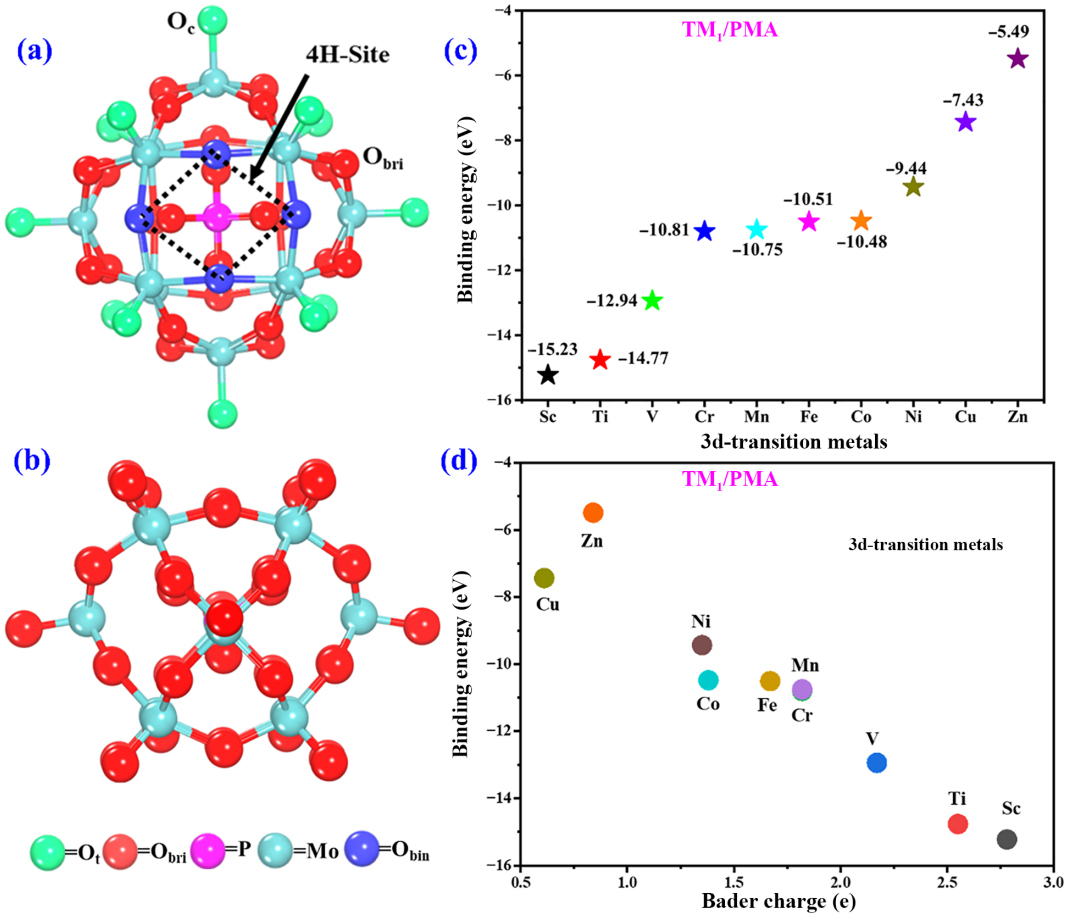


Figure 1 (a) and (b) Computed geometry in top and side perspectives of PMA cluster. Color code: O_t, green; O_b, red; P, pink, Mo, cyan, O_{bin} (binding-site) blue. (c) The binding energies of TM_1 adatoms on the PMA cluster were calculated and reported in electron volts (eV). (d) Relationship between the Bader charge of transition-metal adatoms affixed to the PMA cluster and the calculated binding energy.

aggregate (Table S2 in the ESM). The charge density variations of the PMA surface integrated with metal atoms illustrate the charge transfer from the metal atoms to the PMA throughout all systems, as demonstrated in Fig. S3 in the ESM, which exhibits substantial charge density depletion and accumulation region between the TM_1 atoms and its adjacent oxygen atoms. It is found that the TM_1/PMA surface rearranges the electron density over the surface, and the electrons are found to localize mainly over the neighbouring oxygen atoms. The Bader charge carried out the quantitative analysis. For the metal atoms in the same periods, the charge transfer decreases with the increase of atomic number (see Fig. 1(d)). Figure 1(d) and Table S2 in the ESM illustrate that the electron transfer from TM_1 atoms to the PMA cluster reduces as the atomic size of the 3d transition metal (TM_1) increases, except for Zn. A strong correlation between charge transfer and binding energies was observed for 3d-TM_1 adsorbed over the PMA cluster. The charge transfer between the metal atoms and the PMA surface is a key factor in the strong binding energies. The findings indicate that electron density is transferred from the TM_1 atoms to the surrounding oxygen atoms, facilitating the stabilization of TM_1 single atoms through partially ionic bonds between TM_1 and oxygen in the TM_1/PMA cluster. Moreover, a positive charge on the TM_1 atoms helps regulate the stability of adsorbed gases, leading to enhanced catalytic reduction of N_2O. The partial density of states (PDOS) for the M-3d, 4s, and O-2p orbitals were analysed to further investigate the binding mechanism. The PDOS plots of all the TM_1/PMA catalysts are presented in Fig. S4 in the ESM. Figure S4 in the ESM shows that the metals 3d and 4s orbitals strongly overlap with the adjacent O-2p orbitals of the PMA cluster. In addition, many sharp peaks of M-3d, 4s, and O-2p orbitals near the Fermi level (E_F), signifying the durable interaction among the TM_1 atoms and the PMA support. The PDOS plots of spin-up and spin-down show that overlapping peaks for TM_1/PMA are asymmetric, suggesting the magnetically active systems. In contrast, TM_1 3d and 4s orbital characteristics around the Fermi level indicate significant reactivity and may be crucial in activating the adsorbates throughout the catalytic process. According to the above results, single metal atoms interact strongly with the 4H sites on the PMA surface, preventing agglomeration. A strong metal-ligand interaction enables the solidification of transition metal atoms by satisfying the empirical requirements of coordination chemistry. Thus, PMA can trap a relatively high quantity of single metal atoms against agglomeration into metal nanoparticles.

Prior work has indicated that efficient adsorption of adsorbates around the active site is an essential feature of an effective catalyst. Carbon dioxide and N_2 are released during the reduction of N_2O by CO molecule. Understanding the CO, N_2O, CO_2, and N_2 adsorption and coadsorption of 2CO and CO+N_2O over TM_1/PMA SACs surface is essential for elucidating the catalytic performance of these catalysts. A wide range of adsorption configurations were investigated for each adsorbate (N_2O and CO) and product (N_2 and CO_2). Figure 2 compares the computed adsorption energies for various gases, while Figs. S5–S11 in the

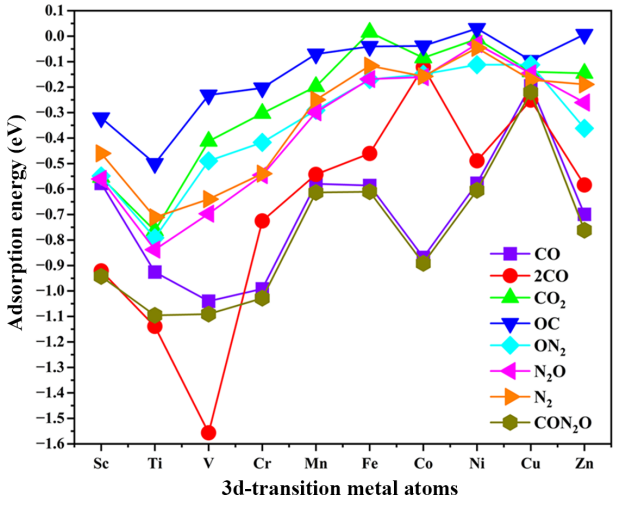


Figure 2 Adsorption and co-adsorption energies (E_{ads} and E_{coads} in eV) of CO (purple), 2CO (red), CO_2 (green), O-end CO (blue), one O-end N_2O (aqua), one N-end (pink), N_2 (orange) and N_2O+CO (olive) on the TM_1/PMA (TM_1= Sc_1, Ti_1, V_1, Cr_1, Mn_1, Fe_1, Co_1, Ni_1, Cu_1, Zn_1) surface at the 4H-site.

ESM illustrates the geometric structure of the most stable configuration. Compared to other gases considered here, CO shows a significant adsorption energy. DFT calculations show that this durable adsorption behavior of the CO molecule presents no metal effects. It is evident that CO significantly inhibits the adsorption of CO_2, N_2, and N_2O. Additionally, since CO molecules strongly adsorb on TM_1/PMA SAC surfaces, the present study did not consider the co-adsorption of CO_2 and N_2 with CO. Our following discussion will focus on the configuration of adsorbing CO and N_2O molecules on TM_1/PMA SACs and mechanism for reduction of N_2O.

The efficiency of a catalyst mainly depends on its ability to bind the reactive molecules efficiently at the catalytic active centres. The adsorption of N_2O and CO molecules on the TM_1/PMA clusters under ambient reaction conditions was investigated first before we investigated the detailed mechanism for reducing N_2O by CO molecules. Consequently, the adsorption energies of N_2O and CO molecules on the TM_1/PMA support were computed. The optimized structures of CO and N_2O on the TM_1/PMA support are presented in Figs. S5 and S7 in the ESM. The adsorption energies and other electronic and structural parameters for N_2O and CO are presented in Fig. 2 and Table S3 in the ESM. The N_2O molecule adsorbed on the TM_1/PMA support primarily through end-on configuration where the N=N-O molecule points toward the metal atom forming the O-TM_1/PMA bond because the higher negative charge on oxygen makes it more favourable for binding. All metal atoms in TM_1/PMA show appreciable adsorption strength with N_2O. The N_2O binds weakly on Cu_1/PMA with an adsorption energy of –0.11 eV, and the strongest contact is observed on Ti_1/PMA with an adsorption energy of –0.79 eV. The adsorption energies of N_2O over the TM_1/PMA support are decreased in the following order of Ti_1 > Sc_1 > V_1 > Cr_1 > Zn_1 > Mn_1 > Fe_1 > Co_1 > Ni_1 > Cu_1, respectively. The bond length of O-N of the adsorbed N_2O gets slightly elongated compared to its free state (1.19 Å), and the N-N bond length is also slightly elongated from 1.11 (free N_2O) to 1.14 Å, respectively. The O-N bond elongation in the adsorbed state occurs owing to the charge transfer from the substrate to the N_2O moiety. The transfer of charge and elongation of bond length activate the N_2O molecule. The transfer of charge density transpires from the TM_1-3d orbital to the 2π* antibonding orbitals of the N_2O molecule, corroborating the notable elongation of the N-O bond length (from 1.19 to 1.21 or 1.23 Å). Consequently, TM_1/PMA is an electron donor, while the N_2O molecule is an electron acceptor. The activation is corroborated by the charge density difference between the TM_1 and O atoms illustrated in Fig. S12 in the ESM. The regions of electron density build-up are depicted in green, encompassing the TM_1 and oxygen atoms, distinctly illustrating the electron transfer from TM_1/PMA to the adsorbed N_2O molecule. The PDOS for N_2O on the TM_1/PMA is illustrated to enhance comprehension of the electrical structure, as shown in Fig. S13 in the ESM. The PDOS indicates that the TM_1 3d orbitals and the O 2p orbital are close to the Fermi level (E_F), suggesting a weak interaction between N_2O and TM_1/PMA. Compared to the PDOS of the TM_1/PMA surface depicted in Fig. S4 in the ESM, the 3d orbitals of TM_1 next to the Fermi level exhibit a modest reduction following the adsorption of N_2O on TM_1/PMA.

We now consider CO adsorption on TM_1/PMA support. Figure S5 in the ESM depicts that the CO prefers the C-bound adsorption mode in which the terminal C atom of CO has a strong bond with the TM_1/PMA support. All the metal atoms in TM_1/PMA show significant binding strength with CO, and the E_{ads} value varies from –0.19 to –1.05 eV. From these calculation results, CO adsorbs weakly on Cu_1/PMA with an adsorption energy of only –0.19 eV and a distance of 2.43 Å between the C and Cu atoms. V_1/PMA has the strongest contact, with an adsorption energy of –1.05 eV. The calculated adsorption energies of CO over TM_1/PMA surface decrease in the following order: V_1 > Cr_1 > Ti_1 > Co_1 > Zn_1 > Fe_1 > Mn_1 > Sc_1 > Ni_1 > Cu_1, respectively. Furthermore, the Dewar–Chatt–Duncanson (DCD) donation and back-donation bonding model results in higher adsorption energy between the TM_1 and CO molecules [70, 71]. We found that the bonding interaction between the TM_1 center and CO molecules occurs in two steps. In the initial step, the lone electron pair in the CO molecule donates electrons to the empty d and s orbitals of the TM_1 atoms. Subsequently, the filled d orbitals of TM_1 interact with the 2π* orbital of the CO molecule, resulting in a reverse charge transfer from the TM_1 center back to the CO molecule. This interaction causes the bond length elongated of the adsorbed CO from 1.11 Å (for free CO) to a range of 1.13–1.16 Å. Bader charge analysis (Table S3 in the ESM) reveals that the TM_1 atoms carry a positive charge, confirming the transfer of charge from the TM_1/PMA surface to the CO molecule, which significantly elongates the C-O bond. The charge transfer and bond length extension activate the CO molecule. This activation is shown in Fig. S14 in the ESM by the charge accumulation zone between the TM_1 and C atoms. To illustrate the electron transfer from TM_1/PMA to adsorbed CO molecule, the electron density accumulation zones covering the TM_1 and carbon atoms are depicted in green. The adsorption of CO onto the TM_1/PMA surface is primarily attributed to the donation of 5σ electrons from CO to the 3d orbital of TM_1 and the back-donation of electrons from the filled 3d orbital of TM_1 to the antibonding 2π* orbital of CO. To better understand the interaction between the TM_1/PMA surface and the CO molecule, we analyzed the PDOS projected onto the 3d orbitals of TM_1 and the 2p orbitals of the carbon and oxygen atoms in CO, as illustrated in Fig. S15 in the ESM. Electrons are transferred from the TM_1 atoms to the empty 2π* orbital of the CO molecule in the gas phase. The partial occupancy of the 2π* orbital somewhat diminishes the C-O bond length. Within the energy range of –10 to –5 eV, the 1π and 5σ orbitals of CO exhibit moderate overlap with the 3d orbital of TM_1 atoms.

The robust hybridization of the 2p orbitals of CO with the 3d orbital of TM_1 aligns with the significant interaction between TM_1/PMA and CO. We observed that all selected TM_1-based PMA catalysts show that CO adsorption is higher than N_2O adsorption. As a result, CO could occupy the active sites on the PMA surface, preventing the adsorption of N_2O and hindering the cleavage of the O-N bond. Therefore, in practical experiments, N_2O is likely to react via the breaking of the O-N bond to generate an active oxygen atom, which subsequently facilitates the oxidation of CO. These results show that adsorption of N_2O and CO molecules on TM_1/PMA was possible from a theoretical viewpoint. Therefore, the TM_1/PMA surface was chosen in this work to study further the catalytic reduction of N_2O by CO molecule under normal reaction conditions. However, all the selected single-atom catalysts have the appropriate adsorption energies, so N_2 and CO_2 molecules can theoretically be produced.

In conclusion, the analysis indicates that CO has a stronger and more favorable adsorption configuration on the TM_1/PMA cluster than N_2O. Additionally, when a CO molecule is already adsorbed on TM_1/PMA, the co-adsorption of a second N_2O molecule at the active site significantly impacts the reaction process. The most stable co-adsorption arrangement of CO and N_2O on TM_1/PMA is depicted in Fig. S16 in the ESM, where N_2O adopts an end-on adsorption mode. Compared to the individual adsorption of CO and N_2O, the co-adsorption binding energies of CO and N_2O are higher on TM_1/PMA, indicating an increased likelihood of co-adsorption, as shown in Fig. 2.

3.2 Reaction mechanism of the N_2O reduction over TM_1/PMA support

N_2O reduction by CO molecule mainly occurs via the following proposed reaction mechanisms.

The adsorption and decomposition of N_2O:

$$N_2O + TM_1/PMA \rightarrow N_2 + O\ldots\ TM_1/PMA$$

The adsorption and oxidation of CO:

$$CO + O\ldots\ TM_1/PMA \rightarrow CO_2 + TM_1/PMA$$

The energetically most favorable configuration of N_2O adsorption on the TM_1/PMA surface is that the N_2O molecule is adsorbed via its oxygen atom. Figure 3 depicts the energy profile for decomposing the N_2O molecule into N_2 and an activated O atom. The optimized geometries related to the breakdown reaction process, encompassing the initial structure (IS1), transition state (TS1), and final state (FS1), are illustrated in Figs. S7, S17 and S18 in the ESM. The chemically adsorbed N_2O on TM_1/PMA is designated the initial structure (IS1), with bond lengths between the TM_1 atoms and the O atom of N_2O ranging from 2.10 to 2.65 Å. In sequence, the breakage of the O-N bond results in the dissociation of N_2O into N_2 molecules through the transition state (TS1). TS1 presents an activation energy barrier ranging from 0.40 to 3.00 eV, along with one imaginary frequency related to the formation of the O-TM_1/PMA bond and the cleavage of the O-N bond. During this process, TM_1-O bond lengths decrease from 2.10–2.65 Å to 1.70–2.00 Å, subsequently to 1.55–2.10 Å, while the O-N bond length increases from 1.21 Å to 2.29 Å via TS1 (Figs. S7, S17 and S18 in the ESM). The linear structure of the adsorbed N_2O molecule is maintained on all selected catalysts. As a result, N_2O decomposed via TS1, leaving active O* on the surface of TM_1/PMA. The N_2O molecule bends from a linear to a V shape in TS1 (bond angle deviates from 180° to 1.37°–145°). Finally, the breaking down the O-N bond yields N_2, and the remaining O atom is still adsorbed over the TM_1/PMA support. Based on the activation energy barrier (E_a) values of Sc_1(2.98 eV), Mn_1(1.92 eV), Co_1(1.03 eV), Ni_1(1.84 eV), Cu_1 (2.92 eV), and Zn_1(2.67 eV), substantial energy is required for these catalysts to catalyze the N_2O decomposition. Surprisingly, Ti_1-, V_1-, Cr_1-, and Fe_1/PMA catalysts revealed respectable catalytic efficiency in the N_2O decomposition and have activation energy barrier values of 0.53, 0.40, 0.85, and 0.94 eV, respectively. Here, TS1(Ti= 444*i* cm^{-1}, V= 482*i* cm^{-1}, Cr= 414*i* cm^{-1}, and Fe= 617i cm^{-1}) has been proven by one imaginary frequency, which is related to the formation of an oxygen-metal bond and the breaking of the O-N bond. Based on the preceding discussion, in what follows, we only consider the Ti_1-, V_1-, Cr_1-, and Fe_1/PMA catalysts when attempting to explore potential candidates for CO oxidation. Due to the weak binding energy, the N_2 molecule leaves the surface, leaving transition metal-oxo (TM_1-O) species intact. This leads to the creation of O-TM_1/PMA, which then acts as a catalyst to oxidize CO further.

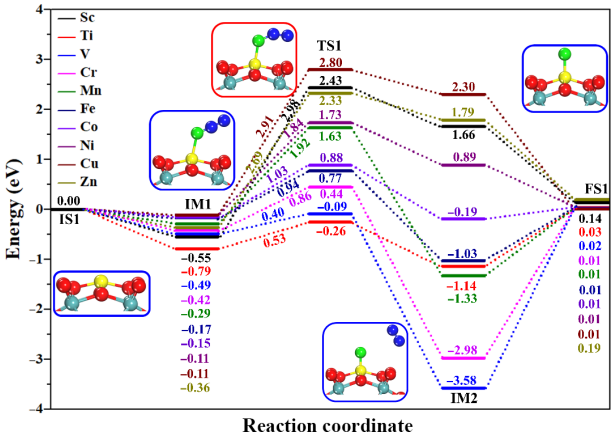


Figure 3 Schematic potential energy profile of the N_2O decomposition over TM_1/PMA (TM_1= Sc_1, Ti_1, V_1, Cr_1, Mn_1, Fe_1, Co_1, Ni_1, Cu_1, Zn_1) surface. All energies are expressed in electronvolts (eV).

After the decomposition of the N_2O molecule, the atomic oxygen remaining on the TM_1/PMA support interacts with the CO molecule. The computed energy profile for the reaction of the remaining O atom (O-TM_1/PMA) with the CO molecule is presented in Fig. 4, and the corresponding initial structure (IS2), transition state (TS2), final state (FS2), and geometrical parameters are shown in Fig. S19 in the ESM. During the catalytic process, the carbon (C) atom from the physically adsorbed CO molecule (IS2) interacts with the remaining O_a atom on the TM_1/PMA surface, producing a CO_2 molecule (FS2) via the transition state (TS2). The catalyst is then regenerated, completing the catalytic cycle. The initial structure (IS2) is based on a parallel configuration of the CO fragment overlaid on the TM_1/PMA support. In this mechanism, the O_a atom separates from the TM_1 adatom as it reacts with CO, creating a CO_2 molecule through the transition state TS2. The calculated activation energy barriers for the IS2 → FS2 transformation are 1.10 eV (527*i* cm^{-1}) for V_1, 0.94 eV (602*i* cm^{-1}) for Cr_1, and 0.43 eV (428*i* cm^{-1}) for Fe_1. During this process, the formation of the C-O bond occurs, accompanied by highly exothermic reactions. Based on the activation energy barrier (E_a) value of V_1(1.10 eV), substantial energy is required for this catalyst to catalyze CO oxidation. Therefore, the above-mentioned catalytic system is not considered a viable catalyst for CO oxidation. In contrast, the Ti_1/PMA might stabilize the oxygen atom and create favorable environments for CO to react

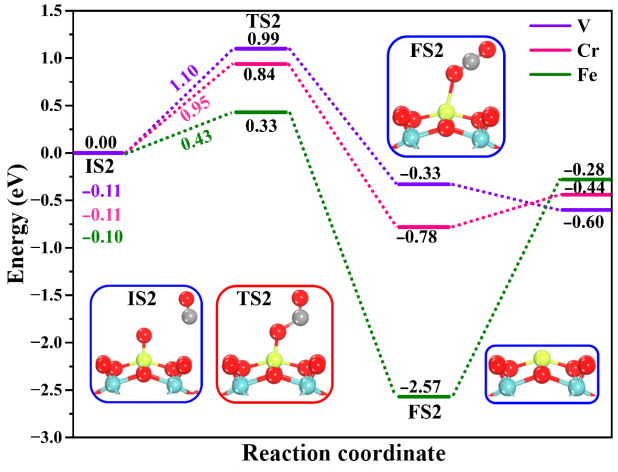


Figure 4 Schematic Potential energy profile of the CO_2 + O* → CO_2 reaction over TM_1/PMA (TM_1= V_1, Cr_1, Fe_1) surface. All energies are expressed in electronvolts (eV).

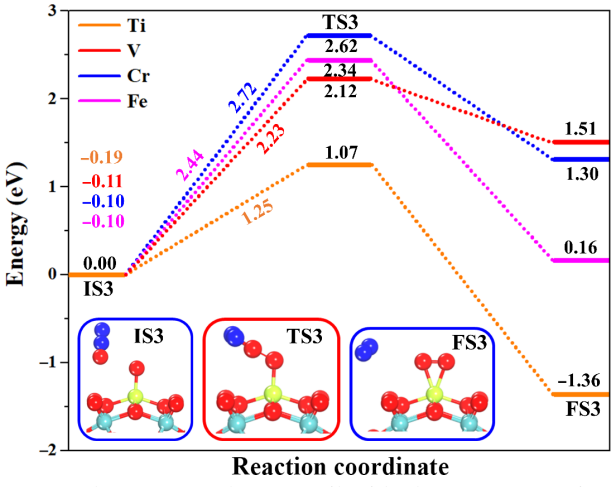


Figure 5 Schematic Potential energy profile of the disproportionation of N_2O molecule over TM_1/PMA (TM_1= Ti_1, V_1, Cr_1, Fe_1) surface. All energies are expressed in electronvolts (eV).

efficiently, releasing CO_2 without any external energy. CO oxidation over the Fe_1/PMA single-atom catalyst (SAC) is achievable under ambient conditions, with an activation energy barrier of 0.43 eV and a single imaginary frequency of 428*i*cm^{-1}. This process involves forming the carbon-oxygen (C-O) bond and breaking the Fe-O bond. At the transition state (TS2), the Fe-O bond length increases from 1.61 to 1.71 Å, while the newly formed C-O bond has a length of 1.57 Å. The resulting CO_2 molecule is weakly adsorbed on the TM_1/PMA surface, enabling it to desorb easily and allowing the catalyst to participate in subsequent CO oxidation cycles.

3.2.1 *N_2O disproportionation on TM_1/PMA support*

We have also investigated the disproportionation of N_2O molecules on the TM_1/PMA support. This reaction involves the interaction of a second N_2O molecule with the remaining O atom over TM_1/PMA. We have considered the following steps.

$$N_2O + O - TM_1/PMA \rightarrow N_2 + O_2 - TM_1/PMA$$

Figure 5 illustrates the computed energy profile for the disproportionation reaction mechanism of N_2O reduction on the TM_1/PMA surface. The optimized geometries corresponding to the initial structure (IS3), transition state (TS3), and final state (FS3) are provided in Fig. S20 in the ESM. The initial structure (IS3) involves a physically adsorbed N_2O molecule, oriented in a parallel configuration, interacting with the remaining O_a atom pre-adsorbed on the TM_1/PMA surface. The N_2O molecule reacts with the remaining O_a atom on the TM_1/PMA support to produce N_2 and O_2 molecules (FS3) via transition state (TS3). The calculated reaction energy barriers for the IS2→FS2 conversion are 1.23 eV (Ti_1), 2.23 eV (V_1), 2.72 eV (Cr_1), and 2.44 eV (Fe_1), respectively. Here, TS3 (Ti= 669*i* cm^{-1}, V= 743*i* cm^{-1}, Cr= 766*i* cm^{-1} and Fe= 899*i* cm^{-1}) has been confirmed by one imaginary frequency, related to the creation of the oxygen-oxygen bond and the dissociation of the nitrogen-oxygen link. It was found that N-O bond distances of N_2O molecules increased in TS3, whereas O-O* interatomic distances decreased (see Fig. S20 in the ESM). Concurrently, the N_2O undergoes a bifurcation to 1.34° (Ti_1), 1.58° (V_1), 1.55° (Cr_1), and 1.48° (Fe_1), and its molecular structure changes from linear to V-shape. The result signifies that due to the significant activation energy barrier, the disproportionation of the N_2O molecule over the TM_1/PMA support does not occur thermodynamically and kinetically at ambient temperature. Moreover, for the N_2O + O* → N_2 + O_2 reaction, the activation energy is higher over TM_1/PMA support because of the robust adsorption of O* species over TM_1/PMA support. Therefore, declining the temperature may hinder the generation of these lateral products over TM_1/PMA. When comparing the first and second dissociations of N_2O through the catalytic cycle, it was revealed that the second dissociation on TM_1-O* had substantially higher energy barriers than the first phase of the N_2O dissociation process on TM_1/PMA. TS3 has a higher activation energy barrier than TS1, which makes it more difficult to use practically. Due to its superior reducibility, CO mostly subsides the reaction after the decomposition of the first N_2O. It is more likely that CO will interact with extra-framework O* and reduce TM_1-active sites than that of N_2O dissociating from TM_1-O*. Previous observations regarding the potential for a disproportionation reaction mechanism of N_2O molecules over various surfaces have verified that this process is kinetically less favorable and should not be desired under experimental conditions [72, 73].

3.2.2 *Concerted reaction mechanism for the co-adsorption of CO and N_2O over TM_1/PMA*

From the discussion as mentioned earlier, we noted that CO is strongly adsorbed over TM_1/PMA with higher adsorption energy than the N_2O molecule. The concerted reaction mechanism involves simultaneous co-adsorption of CO and N_2O molecules over TM_1/PMA support. The concerted reaction mechanism comprises two sequential steps: the reduction of the N_2O molecule by the oxidation of the CO molecule. The co-adsorption of CO and N_2O molecules over the TM_1/PMA surface is considered in the following steps:

$$N_2O + CO + TM_1/PMA \rightarrow N_2O - CO - TM_1/PMA$$

The oxygen transfer:

$$N_2O - CO - TM_1/PMA \rightarrow N_2 + CO_2 + TM_1/PMA$$

Figure 6 presents the potential energy profile, while Fig. S21 in the ESM illustrates the optimized geometries of the initial state (IS4), transition state (TS4), and final state (FS4) for the N_2O reduction through a concerted reaction mechanism. The initial state (IS4) is based on the most stable co-adsorption configuration, where both CO and N_2O molecules are chemically adsorbed on the Ti_1/PMA surface. In contrast, on other catalysts, the N_2O

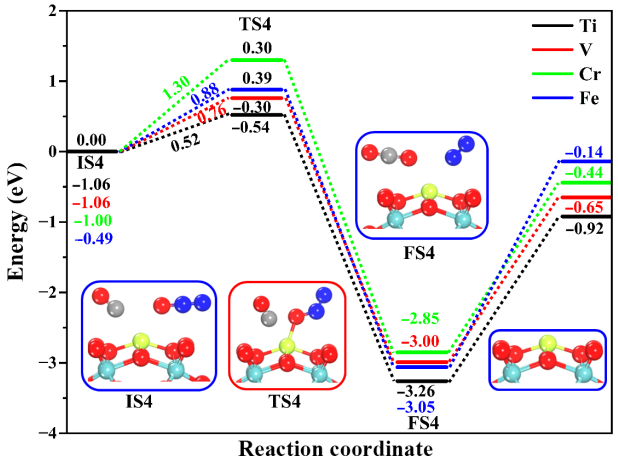


Figure 6 Schematic Potential energy profile of the concerted reaction pathway of the N_2O reduction with CO over TM_1/PMA (TM_1= Ti_1, V_1, Cr_1, Fe_1) surface. All energies are expressed in electronvolts (eV).

molecules are adsorbed physically. As discussed above, CO molecules strongly adsorb over TM_1/PMA surfaces, with higher adsorption energies than N_2O molecules. In contrast, the co-adsorption energy of CO and N_2O is slightly higher than that of CO adsorption except for Sc_1 and Ti_1. This may result from a lack of coordination sites for the M_1 atom and the high adsorption of the CO molecule. In the catalytic reaction, following the co-adsorption of CO and N_2O molecules on the TM_1/PMA surface, the reduction of N_2O occurs concurrently by the transfer of an oxygen atom from N_2O to the CO molecule, resulting in the formation of N_2 and CO_2 molecules (FS4) via the transition state TS4. The TS4 indicates that the oxygen atom dissociates from the nitrogen atom and then associates with the carbon atom, with the activation energy barriers for the (IS4→FS4) conversion being 0.52 eV (Ti_1), 0.76 eV (V_1), 1.30 eV (Cr_1), and 0.89 eV (Fe_1), respectively. The intermolecular bond length of C-O is significantly decreased from 2.98 to 2.57 Å, while the N-O bond length is increased from 1.20 to 1.37 Å. Furthermore, the TM_1 atoms significantly contribute to the attraction of the oxygen atom in N_2O, reducing the TM_1-O bond distance from 3.73 to 3.47 Å. In this instance, TS4 (Ti= 431*i* cm^{-1}, V= 765*i* cm^{-1}, Cr= 611*i* cm^{-1}, and Fe= 876*i* cm^{-1}) has been validated by a single imaginary frequency associated with the transfer of the oxygen atom. Similarly, due to comparatively weak adsorption and significant bond distances (O…TM_1/PMA, N…TM_1/PMA), the generated CO_2 and N_2 molecules will spontaneously desorb from the M_1/PMA at ambient temperature. The reaction selectivity is assessed in both stepwise and coordinated mechanisms. The results reveal that Ti_1- and Fe_1/PMA catalysts demonstrate a strong preference for CO adsorption, which facilitates the co-adsorption of N_2O and drives the concerted oxygen transfer mechanism. The following approaches are suggested to improve reaction efficiency by reducing the strong CO selectivity: introducing one reactant at a time, starting with N_2O for its reduction step, followed by CO for oxidation. However, introducing two reactants sequentially is not practical. In a combined feed, the impact of N_2O should dominate over that of CO. The higher charge of N_2O enables it to adsorb onto the TM_1/PMA catalysts, boosting the reaction rate during the stepwise process and reducing the strong CO adsorption via the concerted reaction mechanism.

Based on all the discussions mentioned above on N_2O reduction catalyzed by TM_1/PMA, it can be concluded that there are significantly fewer energy barriers for two mechanisms (decomposition of N_2O and concerted reaction mechanism). Compared to other chosen catalysts, the results demonstrate that N_2O reduction on Fe_1/PMA SACs is feasible under ambient reaction conditions. Consequently, Fe_1/PMA-supported SACs are theoretically anticipated to be highly reactive catalysts for the N_2O reduction process.

To confirm the sustained activity of the Fe_1/PMA catalyst, the spin magnetic moments offer critical insights into the fundamental steps of the N_2O reduction reaction. Calculations reveal that the Fe_1/PMA catalyst exhibits a spin magnetic moment of 2.90 μ_B at the Fe active site. The crucial stages in the N_2O reduction process include the adsorption of species, the transition states (TSs), and the desorption of reaction products. The determined spin magnetic moment of all the basic steps required in the N_2O reduction via (decomposition of N_2O, oxidation of CO, disproportionation of N_2O, and concerted reaction) mechanisms are presented in Table S4 in the ESM. As discussed above, the spin magnetic moment quenched after the adsorption of N_2O (2.90 to 2.73 μ_B) and CO (2.90 to 0.99 μ_B), which verifies the reduction of unpaired electrons resulting from the hybridization of Fe 3d and O or C 2p orbitals. The results indicate a decrease in the spin magnetic moment across all fundamental stages of N_2O reduction, signifying the reduction of the Fe active center. The desorption of N_2 and CO_2 molecules leads to an increase in the magnetic moments of Fe in FS, resulting in the reoxidation of the Fe active center. Consequently, to evaluate their catalytic efficacy for N_2O reduction, we examined the PDOS for all fundamental steps, with the findings illustrated in Figs. S22–S25 in the ESM. Figures S20–S25 in the ESM clearly demonstrates that the Fe_1 3d orbital significantly influences the variation of the magnetic moment of Fe at all fundamental stages at the Fermi level.

To better understand CO's catalytic reduction of N_2O on the TM_1/PMA cluster, we use transition state theory (TS) to analyze the rate constants (k) for each critical step in the N_2O reduction, N_2O disproportionation, and concerted reaction mechanism. The Boltzmann constant (k_B) is 1.386452×10^{-23} J/K, the Planck's constant (h) is 6.626×10^{-34} js, the activation energy (E_a), the vibrational partition function (q_{TS}) for the transition state, and the main phase of reactants (q_R) are delineated in the equation above. The computation of the vibrational partition function q is as follows:

$$q = \frac{1}{\prod_{i=1}^{\text{vibrations}} \left[-\exp\left(-\frac{h\nu_i}{k_B T} \right) \right]}$$

$$k = \frac{k_B T}{h} \frac{q_{TS}}{q_R} \exp\left[\frac{E_a}{k_B T} \right]$$

In the above equation, ν_i stands for vibrational frequency. For all studied reaction mechanisms, the rate constants are computed at various temperatures (see Tables S5–S7 in the ESM). N_2O reduction and concerted reactions have significantly larger rate constants (k) than all other mechanisms. The DFT simulation indicates that these mechanisms will operate more efficiently than the alternative mechanisms. Concurrently, rate constants for diverse reactions rise with elevated temperatures, suggesting that Ti_1/PMA and Fe_1/PMA may enhance N_2O reduction. In contrast, at 100 K, all the rate constants for all primary phases for the mechanisms underlying these reactions unexpectedly declined, which proves that the cryogenic atmosphere inhibits N_2O reduction with CO. Both kinetically and thermodynamically, Fe_1/PMA offers a better yield of N_2 and CO_2.

4 Conclusion

This work has employed periodic DFT methods to validate the efficacy of transition metal SACs (TM_1=Sc_1, Ti_1, V_1, Cr_1, Mn_1, Fe_1, Co_1, Ni_1, Cu_1, and Zn_1) on a PMA support (TM_1/PMA) for the catalytic reduction of N_2O by CO molecule. Studies indicate that the projected TM_1 single atoms possess appreciable binding energies towards the PMA cluster and are likely to anchor to the fourfold hollow site. Next, we tested their catalytic activity using N_2O reduction. To do this, the adsorption of N_2O and CO molecules on TM_1/PMA systems was considered, and detailed calculations reveal that all systems can be used for the N_2O reduction reaction. Among all the possibilities considered, Ti_1, -V_1, -Cr_1, and Fe_1/PMA catalysts displayed efficient catalytic activity towards the N_2O reduction reaction. It was found that charge transfer from TM_1-3d orbital to $2\pi^*$ orbital of N_2O molecule, which is essential for the decomposition of N_2O molecule. Our results show that CO is more likely to be adsorbed on the TM_1/PMA than N_2O. However, the reaction activity decreased if the CO molecule was first adsorbed on the TM_1/PMA surface. In contrast, when the N_2O molecule was first adsorbed on the TM_1/PMA surface, after the decomposition of N_2O, the CO molecule efficiently reacted with the remaining metal-oxo complex (O-TM_1-PMA), having a lower energy barrier. It was also found that the disproportionation of the N_2O molecule is not possible thermodynamically and kinetically over the TM_1/PMA surface due to the significant activation energy barrier. This reaction can also proceed through a concerted reaction mechanism, which requires an activation energy barrier of 0.52 eV (Ti_1), 0.76 eV (V_1), and 0.89 eV (Fe_1), when the CO molecule was previously adsorbed. We believe Ti_1- and Fe_1/PMA are promising single-atom catalysts for removing the environmentally toxic exhaust gases (NO, CO, and N_2O) produced from industrial and vehicle wastes. These results will benefit the experimentalist in synthesizing TM_1-anchored PMA cluster single-atom catalysts for the N_2O reduction reactions.

Acknowledgements

We acknowledge financial support for this work from the Center for Catalysis and Separations (CeCaS). The theoretical calculations were performed using the high-performance computing clusters of Khalifa University. The authors would like to acknowledge the support of the research computing department of Khalifa University.

Electronic Supplementary Material: Supplementary material (the details of the optimized geometry of PMA with various possible coordination sites, binding energies (eV), cohesive energies (eV), Bader charge, adsorption energies (eV), bond lengths, charge density differences, spin-polarized PDOS, optimized geometries of adsorbates and intermediates, magnetic moment and rate constant) is available in the online version of this article at https://doi.org/10.26599/NRE.2025.9120158.

Author contributions

S.H.T. designed the catalyst and wrote the initial manuscript. S.H.T., A.Q. and S.M. performed the density function theory (DFT) calculations and data analysis. B.A. and A.H.D. in discussing and editing the manuscripts. J.L. and S.M. supervised the project and organized the collaboration.

Declaration of conflicting interests

The authors declare no conflicting interests regarding the content of this article.

Data availability

All data needed to support the conclusions in the paper are presented in the manuscript and/or the Supplementary Materials. Additional data related to this paper may be requested from the corresponding author upon request.

References

[1] Thakur, I. S.; Kristina, M. Nitrification and denitrification processes for mitigation of nitrous oxide from waste water treatment plants for biovalorization: Challenges and opportunities. *Bioresour. Technol.* **2019**, *282*, 502–513.

[2] Ma, J. B.; Wang, Z. C.; Schlangen, M.; He, S. G.; Schwarz, H. On the origin of the surprisingly sluggish redox reaction of the N_2O/CO couple mediated by $[Y_2O_2]^+$ and $[YAlO_2]^+$ cluster ions in the gas phase. *Angew. Chem., Int. Ed.* **2013**, *52*, 1226–1230.

[3] Ravishankara, A. R.; Daniel, J. S.; Portmann, R. W. Nitrous oxide (N_2O): The dominant ozone-depleting substance emitted in the 21st century. *Science* **2009**, *326*, 123–125.

[4] Dameris, M. Depletion of the ozone layer in the 21st century. *Angew. Chem., Int. Ed.* **2010**, *49*, 489–491.

[5] Gorguner, M.; Akgun, M. Acute inhalation injury. *Eurasian J. Med.* **2010**, *42*, 28–35.

[6] Krug, E. C.; Frink, C. R. Acid rain on acid soil: A new perspective. *Science* **1983**, *221*, 520–525.

[7] Liu, Z. P.; Hu, P. CO oxidation and NO reduction on metal surfaces: Density functional theory investigations. *Top. Catal.* **2004**, *28*, 71–78.

[8] Gong, X. Q.; Liu, Z. P.; Raval, R.; Hu, P. A systematic study of CO oxidation on metals and metal oxides: Density functional theory calculations. *J. Am. Chem. Soc.* **2004**, *126*, 8–9.

[9] Zeng, R.; Feller, M.; Diskin-Posner, Y.; Shimon, L. J. W.; Ben-David, Y.; Milstein, D. CO oxidation by N_2O homogeneously catalyzed by ruthenium hydride pincer complexes indicating a new mechanism. *J. Am. Chem. Soc.* **2018**, *140*, 7061–7064.

[10] Blagojevic, V.; Orlova, G.; Bohme, D. K. O-atom transport catalysis by atomic cations in the gas phase: Reduction of N_2O by CO. *J. Am. Chem. Soc.* **2005**, *127*, 3545–3555.

[11] Nematollahi, P.; Esrafili, M. D. A DFT study on the N_2O reduction by CO molecule over silicon carbide nanotubes and nanosheets. *RSC Adv.* **2016**, *6*, 59091–59099.

[12] Montzka, S. A.; Dlugokencky, E. J.; Butler, J. H. Non-CO_2 greenhouse gases and climate change. *Nature* **2011**, *476*, 43–50.

[13] Pérez-Ramírez, J. Prospects of N_2O emission regulations in the European fertilizer industry. *Appl. Catal. B Environ.* **2007**, *70*, 31–35.

[14] Tolman, W. B. Binding and activation of N_2O at transition-metal centers: Recent mechanistic insights. *Angew. Chem., Int. Ed.* **2010**, *49*, 1018–1024.

[15] Smirnov, V. N.; Akhmadov, U. S. Reactions of Cr atoms with NO, N_2O, CO_2, NO_2, and SO_2 molecules. *Kinet. Catal.* **2010**, *51*, 617–623.

[16] Zhao, L. M.; Liu, Z. C.; Guo, W. Y.; Zhang, L. Z.; Zhang, F. Y.; Zhu, H. Y.; Shan, H. H. Theoretical investigation of the gas-phase Mn^+- and Co^+-catalyzed oxidation of benzene by N_2O. *Phys. Chem. Chem. Phys.* **2009**, *11*, 4219–4229.

[17] Najafi, M. P-doped carbon nanotube and Ge-doped boron nitride nanotube as a real catalyst for N_2O + SiO reaction: DFT examination. *Appl. Surf. Sci.* **2017**, *420*, 243–251.

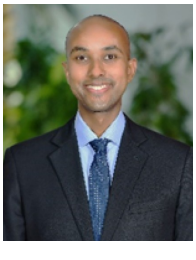
[18] Esrafili, M. D.; Saeidi, N. N_2O+SO_2 reaction over Si- and C-doped boron nitride nanotubes: A comparative DFT study. *Appl. Surf. Sci.* **2017**, *403*, 43–50.

[19] Arenas-Alatorre, J.; Gómez-Cortés, A.; Avalos-Borja, M.; Díaz, G. Surface properties of Ni−Pt/SiO_2 catalysts for N_2O decomposition and reduction by H_2. *J. Phys. Chem. B* **2005**, *109*, 2371–2376.
[20] Oktar, N.; Mitome, J.; Holmgreen, E. M.; Ozkan, U. S. Catalytic reduction of N_2O and NO_2 with methane over sol-gel palladium-based catalysts. *J. Mol. Catal. A Chem.* **2006**, *259*, 171–182.
[21] Giese, P.; Kirsch, H.; Wolf, M.; Frischkorn, C. Reduction of N_2O on MgO/Ag(100) via UV-photoinduced trapped electrons. *J. Phys. Chem. C* **2011**, *115*, 10012–10018.
[22] Sobolev, V. I.; Pirutko, L. V. Room temperature reduction of N_2O by CO over Au/TiO_2. *Catal. Commun.* **2012**, *18*, 147–150.
[23] Pirngruber, G. D.; Frunz, L.; Pieterse, J. A. Z. The synergy between Fe and Ru in N_2O decomposition over FeRu-FER catalysts: A mechanistic explanation. *J. Catal.* **2006**, *243*, 340–349.
[24] Shan, J. J.; Zhu, Y.; Zhang, S. R.; Zhu, T.; Rouvimov, S.; Tao, F. Catalytic performance and *in situ* surface chemistry of pure α-MnO_2 nanorods in selective reduction of NO and N_2O with CO. *J. Phys. Chem. C* **2013**, *117*, 8329–8335.
[25] Gholizadeh, R.; Yu, Y. X. N_2O+CO reaction over Si- and Se-doped graphenes: An *ab initio* DFT study. *Appl. Surf. Sci.* **2015**, *357*, 1187–1195.
[26] Kappes, M. M.; Staley, R. H. Oxidation of transition-metal cations in the gas phase. Oxygen bond dissociation energies and formation of an excited-state product. *J. Phys. Chem.* **1981**, *85*, 942–944.
[27] Kappes, M. M.; Staley, R. H. Gas-phase oxidation catalysis by transition-metal cations. *J. Am. Chem. Soc.* **1981**, *103*, 1286–1287.
[28] Qiao, B. T.; Wang, A. Q.; Yang, X. F.; Allard, L. F.; Jiang, Z.; Cui, Y. T.; Liu, J. Y.; Li, J.; Zhang, T. Single-atom catalysis of CO oxidation using Pt_1/FeO_x. *Nat. chem.* **2011**, *3*, 634–641.
[29] Wang, A. Q.; Li, J.; Zhang, T. Heterogeneous single-atom catalysis. *Nat. Rev. Chem.* **2018**, *2*, 65–81.
[30] Li, Z.; Ji, S. F.; Liu, Y. W.; Cao, X.; Tian, S. B.; Chen, Y. J.; Niu, Z. Q.; Li, Y. D. Well-defined materials for heterogeneous catalysis: From nanoparticles to isolated single-atom sites. *Chem. Rev.* **2020**, *120*, 623–682.
[31] Liu, J. C.; Tang, Y.; Wang, Y. G.; Zhang, T.; Li, J. Theoretical understanding of the stability of single-atom catalysts. *Natl. Sci. Rev.* **2018**, *5*, 638–641.
[32] Zhu, C. Z.; Fu, S. F.; Shi, Q. R.; Du, D.; Lin, Y. H. Single-atom electrocatalysts. *Angew. Chem., Int. Ed.* **2017**, *56*, 13944–13960.
[33] Pan, Y.; Lin, R.; Chen, Y. J.; Liu, S.; Zhu, W.; Cao, X.; Chen, W. X.; Wu, K. L.; Cheong, W. C.; Wang, Y. et al. Design of single-atom Co–N_5 catalytic site: A robust electrocatalyst for CO_2 reduction with nearly 100% CO selectivity and remarkable stability. *J. Am. Chem. Soc.* **2018**, *140*, 4218–4221.
[34] Hülsey, M. J.; Zhang, B.; Ma, Z. R.; Asakura, H.; Do, D. A.; Chen, W.; Tanaka, T.; Zhang, P.; Wu, Z. L.; Yan, N. *In situ* spectroscopy-guided engineering of rhodium single-atom catalysts for CO oxidation. *Nat. Commun.* **2019**, *10*, 1330.
[35] Zheng, S. T.; Yang, G. Y. Recent advances in paramagnetic-TM-substituted polyoxometalates (TM = Mn, Fe, Co, Ni, Cu). *Chem. Soc. Rev.* **2012**, *41*, 7623–7646.
[36] Jia, Y.; Zhang, J.; Zhang, Z. M.; Li, Q. Y.; Wang, E. B. Metal-centered polyoxometalates encapsulated by surfactant resulting in the thermotropic liquid crystal materials. *Inorg. Chem. Commun.* **2014**, *43*, 5–9.
[37] Blazevic, A.; Rompel, A. The Anderson-Evans polyoxometalate: From inorganic building blocks via hybrid organic-inorganic structures to tomorrows "Bio-POM". *Coord. Chem. Rev.* **2016**, *307*, 42–64.
[38] Bijelic, A.; Rompel, A. The use of polyoxometalates in protein crystallography-An attempt to widen a well-known bottleneck. *Coord. Chem. Rev.* **2015**, *299*, 22–38.
[39] Talib, S. H.; Jiang, X. L.; Feng, S. X.; Zhao, M. D.; Yu, Q. Theoretical catalytic performance of single-atom catalysts $M_1/PW_{12}O_{40}$ for alkyne hydrogenation materials. *Nano Res. Energy* **2024**, *3*, e9120128.
[40] Bashir, B.; Talib, S. H.; Khan, M. A.; Mohamed, S.; Qurashi, A.; Xiao, H.; Li, J. Enhancing direct hydroxylation of benzene to phenol on Fe_1/PMA single-atom catalyst: A comparative study of H_2O_2 vs. O_2-assisted reactions. *Mater. Adv.* **2024**, *5*, 5458–5470.
[41] Hussain, S.; Talib, S. H.; Ali, B.; Mohamed, S.; Qurashi, A.; Li, J.; Lu, Z. S. Single-atom electrocatalysts anchored on phosphoniobic acid ($M_1/PNb_{12}O_{40}$) cluster for water splitting (HER/OER) and metal-air batteries (ORR). *ACS Mater. Lett.* **2024**, *6*, 2311–2319.
[42] Hussain, S.; Talib, S. H.; Shahzad, S. R.; Muhammad, S.; Mohamed, S.; Qurashi, A.; Wang, H. Y.; Lu, Z. S. Heterogeneous $Co_1/P_1Mo_{12}O_{40}$ single-atom catalyst for CO oxidation via termolecular Eley-Rideal (TER) mechanism. *Mol. Catal.* **2023**, *550*, 113539.
[43] Zhang, B.; Asakura, H.; Zhang, J.; Zhang, J. G.; De, S.; Yan, N. Stabilizing a platinum1 single-atom catalyst on supported phosphomolybdic acid without compromising hydrogenation activity. *Angew. Chem., Int. Ed.* **2016**, *55*, 8319–8323.
[44] Yin, Y. Q.; Jiang, M. X.; Liu, C. G. DFT study of POM-supported single atom catalyst (M_1/POM, M = Ni, Pd, Pt, Cu, Ag, Au, POM = $[PW_{12}O_{40}]^{3-}$) for activation of nitrogen molecules. *Acta Phys. Chim. Sin.* **2018**, *34*, 270–277.
[45] Liu, C. G.; Jiang, M. X.; Su, Z. M. Computational study on M_1/POM single-atom catalysts (M = Cu, Zn, Ag, and Au; POM = $[PW_{12}O_{40}]^{3-}$): Metal-support interactions and catalytic cycle for alkene epoxidation. *Inorg. Chem.* **2017**, *56*, 10496–10504.
[46] Zhang, B.; Asakura, H.; Yan, N. Atomically dispersed rhodium on self-assembled phosphotungstic acid: Structural features and catalytic CO oxidation properties. *Ind. Eng. Chem. Res.* **2017**, *56*, 3578–3587.
[47] Yu, M. A.; Feng, Y. X.; Gao, L. Y.; Lin, S. Phosphomolybdic acid supported single-metal-atom catalysis in CO oxidation: First-principles calculations. *Phys. Chem. Chem. Phys.* **2018**, *20*, 20661–20668.
[48] Wang, S. J.; Feng, Y. X.; Lin, S.; Guo, H. Phosphomolybdic acid supported atomically dispersed transition metal atoms (M = Fe, Co, Ni, Cu, Ru, Rh, Pd, Ag, Os, Ir, Pt, and Au): Stable single atom catalysts studied by density functional theory. *RSC Adv.* **2017**, *7*, 24925–24932.
[49] Talib, S. H.; Yu, X. H.; Yu, Q.; Baskaran, S.; Li, J. Non-noble metal single-atom catalysts with phosphotungstic acid (PTA) support: A theoretical study of ethylene epoxidation. *Sci. China Mater.* **2020**, *63*, 1003–1014.
[50] Talib, S. H.; Yu, X. H.; Lu, Z. S.; Ahmad, K.; Yang, T. T.; Xiao, H.; Li, J. A polyoxometalate cluster-based single-atom catalyst for NH_3 synthesis via an enzymatic mechanism. *J. Mater. Chem. A* **2022**, *10*, 6165–6177.
[51] Talib, S. H.; Lu, Z. S.; Yu, X. H.; Ahmad, K.; Bashir, B.; Yang, Z. X.; Li, J. Theoretical inspection of M_1/PMA single-atom electrocatalyst: Ultra-high performance for water splitting (HER/OER) and oxygen reduction reactions (OER). *ACS Catal.* **2021**, *11*, 8929–8941.
[52] Kresse, G.; Furthmüller, J. Efficiency of *ab-initio* total energy calculations for metals and semiconductors using a plane-wave basis set. *Comput. Mater. Sci.* **1996**, *6*, 15–50.
[53] Kresse, G.; Hafner, J. *Ab initio* molecular dynamics for liquid metals. *Phys. Rev. B* **1993**, *47*, 558(R)–561(R).
[54] Kresse, G. *Ab initio* molecular dynamics for liquid metals. *J. Non. Cryst. Solids.* **1995**, *192−193*, 222–229.
[55] Kresse, G.; Joubert, D. From ultrasoft pseudopotentials to the Projector-Augmented-Wave method. *Phys. Rev. B* **1999**, *59*, 1758–1775.
[56] Maniopoulou, A.; Davidson, E. R. M.; Grau-Crespo, R.; Walsh, A.; Bush, I. J.; Catlow, C. R. A.; Woodley, S. M. Introducing *k*-point parallelism into VASP. *Comput. Phys. Commun.* **2012**, *183*, 1696–1701.
[57] Torrent, M.; Jollet, F.; Bottin, F.; Zérah, G.; Gonze, X. Implementation of the Projector-Augmented-Wave method in the ABINIT code: Application to the study of iron under pressure. *Comput. Mater. Sci.* **2008**, *42*, 337–351.
[58] Jollet, F.; Torrent, M.; Holzwarth, N. Generation of projector

augmented-wave atomic data: A 71 element validated table in the XML format. *Comput. Phys. Commun.* **2014**, *185*, 1246–1254.
[59] Perdew, J. P.; Burke, K.; Ernzerhof, M. Generalized gradient approximation made simple. *Phys. Rev. Lett.* **1996**, *77*, 3865–3868.
[60] Perdew, J. P.; Burke, K.; Ernzerhof, M. Perdew, burke, and ernzerhof reply. *Phys. Rev. Lett.* **1998**, *80*, 891.
[61] Zhang, Y. K.; Yang, W. T. Comment on "generalized gradient approximation made simple". *Phys. Rev. Lett.* **1998**, *80*, 890.
[62] Tang, W.; Sanville, E.; Henkelman, G. A grid-based Bader analysis algorithm without lattice bias. *J. Phys. Condens. Matter* **2009**, *21*, 084204.
[63] Sanville, E.; Kenny, S. D.; Smith, R.; Henkelman, G. Improved grid-based algorithm for Bader charge allocation. *J. Comput. Chem.* **2007**, *28*, 899–908.
[64] Yu, M.; Trinkle, D. R. Accurate and efficient algorithm for Bader charge integration. *J. Chem. Phys.* **2011**, *134*, 064111.
[65] Henkelman, G.; Uberuaga, B. P.; Jónsson, H. A climbing image nudged elastic band method for finding saddle points and minimum energy paths. *J. Chem. Phys.* **2000**, *113*, 9901–9904.
[66] Zarkevich, N. A.; Johnson, D. D. Nudged-elastic band method with two climbing images: Finding transition states in complex energy landscapes. *J. Chem. Phys.* **2015**, *142*, 024106.
[67] Henkelman, G.; Jónsson, H. A dimer method for finding saddle points on high dimensional potential surfaces using only first derivatives. *J. Chem. Phys.* **1999**, *111*, 7010–7022.
[68] Heyden, A.; Bell, A. T.; Keil, F. J. Efficient methods for finding transition states in chemical reactions: Comparison of improved dimer method and partitioned rational function optimization method. *J. Chem. Phys.* **2005**, *123*, 224101.
[69] Kästner, J.; Sherwood, P. Superlinearly converging dimer method for transition state search. *J. Chem. Phys.* **2008**, *128*, 014106.
[70] Chatt, J.; Duncanson, L. A. 586. Olefin co-ordination compounds. Part III. Infra-red spectra and structure: Attempted preparation of acetylene complexes. *J. Chem. Soc.* **1953**2939–2947.
[71] Chatt, J.; Duncanson, L. A.; Venanzi, L. M. Directing effects in inorganic substitution reactions. Part I. A hypothesis to explain the trans-effect. *J. Chem. Soc.* **1955**, *1*, 4456–4460.
[72] Khan, A. A.; Alsalhi, S. A.; Rahman, A. U. Exploring Si-centered phthalocyanine as a single atom catalyst for N_2O reduction: A DFT study. *Phys. Chem. Chem. Phys.* **2024**, *26*, 17110–17117.
[73] Song, E. H.; Yan, J. M.; Lian, J. S.; Jiang, Q. External electric field catalyzed N_2O decomposition on Mn-embedded graphene. *J. Phys. Chem. C* **2012**, *116*, 20342–20348.



Shamraiz Hussain Talib received his PhD degree from the Department of Chemistry and Key Laboratory of Organic Optoelectronics & Molecular Engineering, Tsinghua University, under the supervision of Prof. Jun Li. He did postdoctoral research at the Henan Normal University (China) in 2022. He is now a postdoctoral research fellow at Khalifa University's Center for Catalysis and Separations (CeCaS) under the supervision of Prof. Sharmarke Mohamed. His research involves theoretical chemistry and computational catalysis science.



Sharmarke Mohamed is an Associate Professor of Chemistry, theme leader in the Center for Catalysis and Separations (CeCaS) and PI of the Green Chemistry & Materials Modelling (GCMM) Laboratory at Khalifa University. In 2011, he received his PhD from UCL. His PhD research focused on small molecule X-ray crystallography and computational methods of crystal structure prediction. He has worked in the pharmaceutical industry as an experimental drug development chemist and is an inventor on a number of patents. Since joining the faculty at Khalifa University in 2014, he has widened his research interests to cover mechanochemistry, multiscale materials modelling and green chemistry.